In vivo brain imaging using a portable 3.9 gram two-photon fluorescence microendoscope

Benjamin A. Flusberg, Juergen C. Jung, Eric D. Cocker, Erik P. Anderson, and Mark J. Schnitzer

James H. Clark Center for Biomedical Engineering & Sciences, Stanford University, Stanford, California 94305-5435

Received May 6, 2005; revised manuscript received June 27, 2005; accepted June 30, 2005

We introduce a compact two-photon fluorescence microendoscope based on a compound gradient refractive index endoscope probe, a DC micromotor for remote adjustment of the image plane, and a flexible photonic bandgap fiber for near distortion-free delivery of ultrashort excitation pulses. The imaging head has a mass of only 3.9 g and provides micrometer-scale resolution. We used portable two-photon microendoscopy to visualize hippocampal blood vessels in the brains of live mice. © 2005 Optical Society of America

OCIS codes: 170.2150, 170.2520, 170.5810, 170.3880, 110.2350, 110.2760.

Fluorescence microendoscopy (FME) is an emerging imaging modality that enables visualization of biological cells within tissues too deep to access by conventional microscopy.[1–4] FME can involve one-[2] or two-photon fluorescence excitation,[1–3,5,6] and these forms have distinct strengths and weaknesses.[4] Two-photon FME provides inherent optical sectioning deep within scattering tissue but requires laser scanning.[2–4] Microendoscope probes composed of compound gradient refractive index (GRIN) lenses have enabled imaging of individual neurons within deep brain areas by use of two-photon FME.[2,3] In these studies the instrumentation resembled a conventional two-photon microscope but with a minimally invasive optical relay for insertion into tissue.[2,3] This limits applications because the specimen must be immobilized.

Many research and clinical applications would benefit from two-photon imaging devices that are compact and mobile. Toward this end, a GRIN probe mated to an optical fiber bundle provides improved mechanical flexibility,[6] but the bundle degrades image quality due to pixilation and distorts the ultrashort pulses of energies above ~0.1 nJ that are commonly used for two-photon excitation.[7,8] Ideally, ultrashort pulse delivery should involve single-mode propagation in optical fibers that reduce[7,8] or nearly eliminate[9] pulse distortion due to self-phase modulation (SPM). We introduce a portable two-photon microendoscope based on a flexible photonic bandgap fiber, in which the lowest-order mode travels in an air core. The imaging head, including a fiber scanner and two focusing mechanisms, displays a mass of 3.9 g—considerably smaller than prior forms of fiber-scanning two-photon microscopy.[10]

Figure 1(a) provides an optical schematic of the imaging head. To deliver excitation light we coupled pulses (100–150 fs, center wavelength 790–810 nm) from a Ti:sapphire laser into the lowest-order mode of the bandgap fiber [Fig. 1(b)]. Unlike in conventional single-mode fiber (SMF), this mode enables ultrashort pulse transmission virtually free of SPM, because the optical Kerr coefficient is insignificant within the air core.[9] Group velocity dispersion (GVD) in the fiber vanishes at ~795 nm, so our pulses propagate nearly free of GVD. Light exiting the fiber reflects off a coated 1 mm microprism serving as a dichroic mirror and into a 1-mm-diameter doublet GRIN lens probe that focuses the light into the sample [Fig. 1(a)]. The GRIN probe comprises an endoscopic objective lens (0.48 NA, 0.22 pitch) and relay lens (0.2 NA, 0.14 pitch or 0.11 NA, 0.18 pitch). A multimode polymer fiber (980-μm-diameter core, 0.51 NA) positioned above the microprism captures fluorescence photons returning through the endoscope probe.

To scan laterally across the image field, we used a piezoelectric actuator to drive resonant vibrations in an overhang of the delivery fiber.[10] A short piece of bare fiber connecting the actuator to the delivery fiber splits the two resonant frequencies of lateral vibration [Fig. 1(a)]. Driving the actuator with a voltage signal containing both resonant frequencies drives the tip of the bandgap fiber in a Lissajous pat-

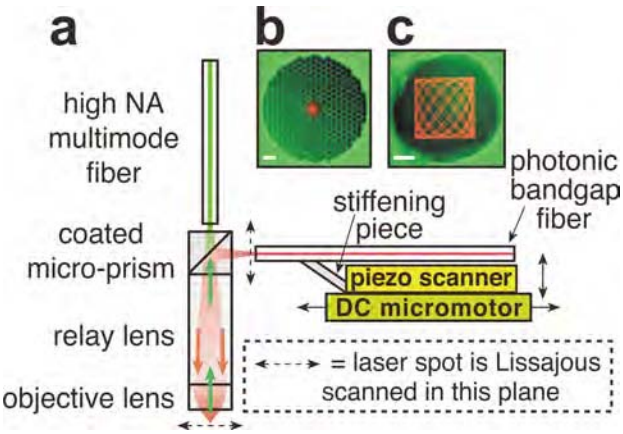

Fig. 1. a, Schematic of the imaging head. Arrows extending from the micromotor and scanner indicate directions of movement. b, Photographic overlay of near-field intensity distribution of infrared light in the lowest-order mode (red pseudocolor) exiting the bandgap fiber (green pseudocolor). The scale bar is 10 μm. The mode appears off center from the 6.8-μm-diameter air core due to a small shift between image acquisitions. c, Endoscope probe (green pseudocolor) and a real image of the Lissajous scanning pattern (red pseudocolor) that arises from a reflection at the junction of the GRIN objective and relay lenses. The Lissajous driving frequencies were 538 and 698 Hz. Only a portion of the pattern appears due to an image acquisition time of 0.067 s. The scale bar is 200 μm.

0146-9592/05/172272-3/$15.00

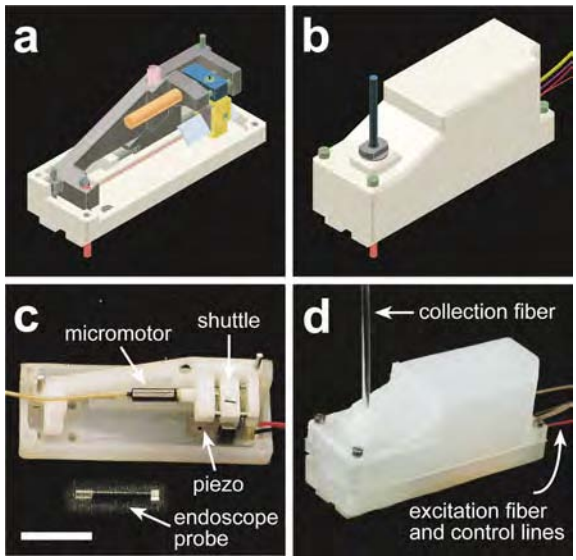

Fig. 2. a, Computer-aided-design (CAD) model of device components mounted on the baseplate. White, baseplate (nylon); red, endoscope probe and bandgap fiber; light blue, piezo actuator; gold, piezo clip (titanium); gray, wedge mechanism for coarse focusing (acetal); pink, spring for wedge mechanism; orange, micromotor; blue, micromotor shuttle (acetal) for finer focusing; green, screws and rails (stainless steel). b, CAD model of the imaging head. White, baseplate and casing (nylon); blue, fluorescence collection fiber; green, screws (stainless steel). The bandgap fiber (pink), actuator leads (red and purple), and motor control lines (yellow) exit through a slot in the casing. c, Photograph of components assembled as in panel a. Scale bar is 1 cm. d, Photograph of the imaging head.

tern [Fig. 1(c)]. Similar Lissajous scanning mechanisms have been used previously for fiber-optic imaging.[10–12] The ratio of the driving frequencies determines the sampling density. Although the image periphery is oversampled compared to the center, this effect is easily corrected online in software. We chose driving frequencies near the resonance peaks that led to minimal mechanical cross talk between vibrational modes. The Lissajous pattern is demagnified by 3.2–5.2× at the sample and can be adjusted in size by setting the amplitude of the drive voltages [Fig. 1(c)]. Maximum scan fields are up to ~145–215 μm in extent, depending on the endoscope probe used. To adjust the image focus a DC micromotor [Figs. 2(a) and 2(c)] moves the entire scanning assembly, held in a shuttle, along a threaded shaft. Varying the distance between the fiber tip and microprism in this manner over a full range of 1.5 mm yields axial focal shifts of up to ~145 μm.

A modular casing secures the optical and electronic components on a baseplate [Figs. 2(a) and 2(c)]. For alignment of the bandgap fiber, the piezoelectric actuator pivots in two dimensions about its attachment to the shuttle. A wedge mechanism adjusts the height of the optical assembly and the distance that the GRIN probe protrudes beyond the baseplate. This permits coarse focal control. A cap holding the multimode fiber [Figs. 2(b) and 2(d)] can be removed to allow conventional epifluorescence imaging through the microprism and the endoscope probe using a microscope objective. In this mode, the microprism transmits visible excitation and emission light, allowing rapid assessment of whether fluorescent objects are in the field of view prior to laser-scanning imaging. The entire imaging head is ~3.5 cm × 1.2 cm × 1.5 cm and has a mass of 3.9 g.

To confirm near distortion-free pulse delivery, we measured the pulse duration after propagation through the bandgap fiber and endoscope probe [Fig. 3(a)]. Pulses suffered slight temporal broadening in the fiber [Fig. 3(a)], perhaps in part due to modal dispersion from surface modes.[13] Broadening due to higher-order GVD might also occur. For pulses of initial width $\tau_0 = 100-150$ fs, the characteristic third-order dispersion length, $L_D' = \tau_0^3/|\beta_3|$ (Ref. 14) is ~0.6–2 m at the zero-GVD wavelength of our bandgap fiber, ~10–20 times shorter than in conventional SMF.[14]

To study imaging resolution, we visualized 100-nm-diameter fluorescent beads [Fig. 3(b)]. The lateral and axial resolution limits of the portable imaging device, as estimated by the FWHM of curve fits to bead images, are 1.21 ± 0.04 μm (mean ± SEM, $n = 9$) and 9.8 ± 0.5 μm ($n = 3$), respectively. These values approach those exhibited by the endoscope probe alone (lateral FWHM, 1.01 ± 0.04 μm ($n = 6$); axial FWHM, 8.0 ± 0.5 μm ($n = 3$), [Fig. 3(b)]) and are comparable to previous microendoscopy resolution measurements.[1,3] The minor degradation in resolution from that afforded by the probe alone arises because light exiting the bandgap fiber underfills the probe. Residual cross talk in the Lissajous pattern might also contribute.

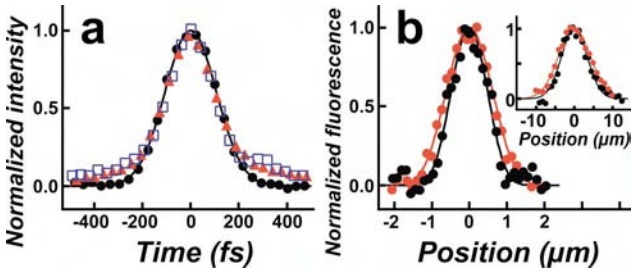

Fig. 3. a, Second-order intensity autocorrelation of laser pulses with spectra centered at 791 nm. Measurements were performed just outside the laser (black circles; solid line, Gaussian fit with $1/e$ width $\tau_0 = 150$ fs), after propagation through 1.5 m of HC-800-02 (Crystal Fibre) bandgap fiber (red triangles), and after propagation through the fiber and a 1.0-cm-long endoscope probe (open blue squares). b, Determination of lateral resolution using normalized line images of single 100-nm-diameter fluorescent beads. Images were acquired in a plane through the axial center of the bead using 802 nm excitation, with the imaging system equipped with a 0.48 NA endoscope probe (red circles), or with the probe alone (black circles). For the latter measurements the excitation beam was expanded to overfill the probe and raster scanned using galvanometer mirrors.[1] Solid lines fits are to the square of an Airy disk.[15] Inset, Determination of axial resolution using amplitudes of fits to a stack of lateral line images, acquired in axial planes spaced either 0.5 or 0.8 μm apart, with the entire imaging system (red circles) or the probe alone (black circles). Solid lines are Gaussian fits.

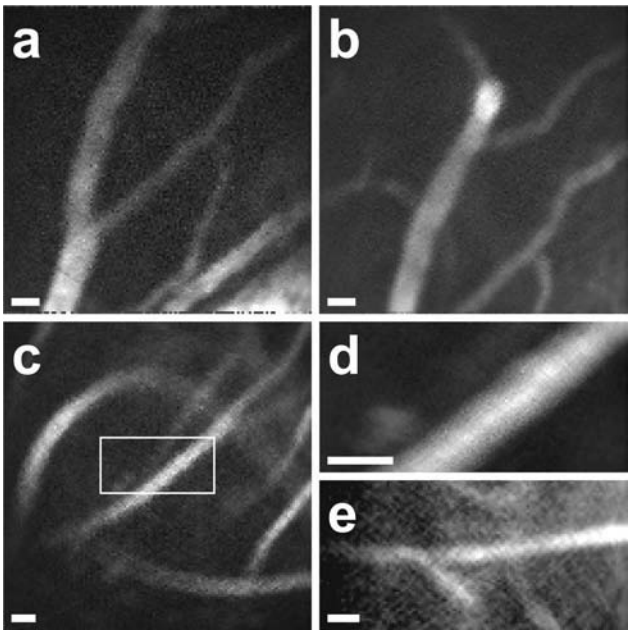

Fig. 4. Images of cerebral blood vessels labeled with fluorescein in anesthetized mice. The frame rate was 2 Hz. a, b, Vessels near the neocortical surface. Excitation power was ~15 mW at the specimen and the endoscope had a working distance (WD) of 250 μm in air. Lissajous driving frequencies were 537 and 699 Hz. c–e, Hippocampal vessels imaged through a 152 μm cover glass at the tip of a guide tube that was implanted just dorsal to hippocampus. The WD was 160 μm in air. Driving frequencies were 538 and 698 Hz. c, Vessels ~20 μm below the dorsal hippocampal surface imaged with ~30 mW power. d, Magnified image of the boxed region in c, obtained by decreasing the Lissajous driving voltages. e, Capillaries ~80 μm below the hippocampal surface imaged with ~80 mW power. Images a–c are 128×128 pixels. Images d and e are 128×62 and 96×46 pixels, respectively. a and c display single image frames, while b, d, and e show averages over six frames. All scale bars are 10 μm.

To demonstrate *in vivo* imaging, we anesthetized adult mice with a ketamine–xylazine cocktail, performed a 2-mm-diameter craniotomy, and injected fluorescein dye into the tail vein.[3,10] This brightly labeled the blood plasma, allowing us to image blood vessels near the neocortical surface [Figs. 4(a) and 4(b)] and up to ~80 μm beneath the dorsal surface of hippocampus [Figs. 4(c)–4(e)].

In summary, we have created a portable two-photon imaging device that exhibits micrometer-scale resolution, focusing capability using a DC micromotor, and a mass of 3.9 g. Such compact instrumentation should be useful for a broad range of biomedical purposes requiring mobile two-photon imaging. Fruitful applications might include clinical diagnostics or studies in small animals.

We thank R. Barretto, T. Brand, M. Digonnet, B. Messerschmidt, M. Solyali, and T. Wang for technical assistance. This work was supported by the Human Frontier Science Program, NSF, and Young Investigator awards to M. Schnitzer from the ONR and the Beckman Foundation. B. Flusberg is an NSF graduate fellow. J. Jung is a Doctor of Philosophy candidate in Pharmacology at Oxford University, Oxford, UK. The Stanford IACUC approved all animal use. Correspondence should be sent to mschnitz@stanford.edu.

References

1. J. C. Jung and M. J. Schnitzer, Opt. Lett. **28**, 902 (2003).
2. J. C. Jung, A. D. Mehta, E. Aksay, R. Stepnoski, and M. J. Schnitzer, J. Neurophysiol. **92**, 3121 (2004).
3. M. J. Levene, D. A. Dombeck, K. A. Kasischke, R. P. Molloy, and W. W. Webb, J. Neurophysiol. **91**, 1908 (2004).
4. A. D. Mehta, J. C. Jung, B. A. Flusberg, and M. J. Schnitzer, Curr. Opin. Neurobiol. **14**, 617 (2004).
5. D. Bird and M. Gu, Opt. Lett. **28**, 1552 (2003).
6. W. Gobel, J. N. Kerr, A. Nimmerjahn, and F. Helmchen, Opt. Lett. **29**, 2521 (2004).
7. D. G. Ouzounov, K. D. Moll, M. A. Foster, W. R. Zipfel, W. W. Webb, and A. L. Gaeta, Opt. Lett. **27**, 1513 (2002).
8. F. Helmchen, D. W. Tank, and W. Denk, Appl. Opt. **41**, 2930 (2002).
9. W. Gobel, A. Nimmerjahn, and F. Helmchen, Opt. Lett. **29**, 1285 (2004).
10. F. Helmchen, M. S. Fee, D. W. Tank, and W. Denk, Neuron **31**, 903 (2001).
11. L. Giniunas, R. Juskaitis, and S. V. Shatalin, Electron. Lett. **27**, 724 (1991).
12. D. L. Dickensheets and G. S. Kino, Proc. SPIE **2184**, 39 (1994).
13. H. K. Kim, M. J. F. Digonnet, G. S. Kino, J. Shin, and S. Fan, Opt. Express **12**, 3436 (2004).
14. G. P. Agrawal, *Nonlinear Fiber Optics*, 3rd ed. (Elsevier Science, San Diego, Calif., 2001).
15. M. Gu and C. J. R. Sheppard, Optik (Stuttgart) **86**, 104 (1990).